IET Journals
The Institution of Engineering and Technology

Measurement-based Geometrical Characterization of the Vehicle-to-Vulnerable-Road-User Communication Channel

ISSN 1751-8644
doi: 0000000000
www.ietdl.org

Ibrahim Rashdan[1]*, *Fabian de Ponte Müller*[1], *Stephan Sand*[1], *Thomas Jost*[1], *Giuseppe Caire*[2]

[1] *German Aerospace Center (DLR), Institute of Communications and Navigation, 82234 Oberpfaffenhofen, Germany*
[2] *Department of Electrical Engineering and Computer Science, Technical University of Berlin, 10623 Berlin, Germany*
✉* *E-mail: ibrahim.rashdan@dlr.de*

Abstract: Vehicle-to-vulnerable road user (V2VRU) communications have the ability to provide 360 degrees of awareness to both vehicles and vulnerable road users (VRUs) to prevent accidents. An accurate V2VRU channel model in critical accident scenarios is essential to develop a reliable communications system. Therefore, extensive wideband single-input and single-output (SISO) channel measurement campaigns at 5.2 GHz were carried out in open-field and urban environments. Accident prone scenarios between a vehicle and a cyclist as well as between a vehicle and a pedestrian are considered. In this paper, locations of the scatterers in the propagation environment are estimated. We propose a method to extract specular MPCs from the estimated time-variant channel impulse response (CIR) based on the density of neighboring MPCs. The specular MPCs are then tracked using a novel tracking algorithm based on the multipath component distance (MCD) approach. Each path is then related to a physical scatterer in the propagation environment by employing a joint delay-Doppler estimation. According to the results, single and double bounce reflections from buildings and parked vehicles are identified in line-of-sight (LoS) situation. In non-LoS (NLoS) situation, scattering from nearby trees as well as reflections from traffic signs and lampposts beneath the trees canopy are identified.

1 Introduction

Globally, around $1.35\,\text{million}$ people die on roads, and more than $50\,\text{million}$ are injured every year [1]. Almost $50\,\%$ of the victims are vulnerable road users (VRUs) i.e., pedestrians, cyclists, and two-wheelers. In the most critical scenarios, where the highest percentage of accidents occurs, the line-of-sight (LoS) between vehicles and VRUs is blocked by obstacles such as buildings and parked vehicles [2]. Therefore, in these scenarios, collision avoidance systems that rely on vehicles on-board sensors such as radars, cameras, and laser scanners are not able to detect VRUs. Direct vehicle-to-vulnerable road user (V2VRU) communications can overcome the limitations of sensor-based systems and provide 360° of awareness for both vehicles and VRUs. V2VRU communications is part of the V2X communications family, which also includes vehicle-to-vehicle (V2V) and vehicle-to-infrastructure (V2I) communications. However, contrary to V2V and V2I [3, 4], V2VRU has not yet received similar attention from researchers.

Accurate channel models are required for developing reliable communications systems. Therefore, a well-founded V2VRU channel model is necessary. To the best of our knowledge, no dedicated channel model for V2VRU communication in critical scenarios is proposed so far. In order to develop a well-founded channel model for V2VRU applications, it is required to conduct wideband channel sounding measurements. Thus, we performed two extensive single-input single-output (SISO) wideband channel measurement campaigns considering vehicle-pedestrian and vehicle-cyclist collision scenarios.

Three main approaches for channel modeling can be found in literature: deterministic, stochastic, and geometry-based stochastic channel models (GSCM). Deterministic approaches, on the one hand, are well known for their accuracy since they are based on detailed modeling of the environment e.g., buildings, vehicles, vegetation and other urban structures. Still, they are in general computational expensive. On the other hand, stochastic channel models depend on channel statistics like Doppler spread or root mean square (RMS) delay spread to model the channel. Such approaches can represent the statistics of the channel. However, they are not able to describe the underlying geometric relations of the propagation channel accurately. The third channel modelling approach achieves a trade-off between accuracy and computational cost. The GSCM approach combines the geometrical and statistical elements providing accurate geometrical relations with a minimal computational burden. In this approach, scatterers are placed randomly according to a distribution. Then, each physical scatterer is associated to a propagation path. A wideband channel model is therefore represented by contributions of all scatterers. The aforementioned trade-off motivates the selection of the GSCM approach for modeling the V2VRU channel. Additionally, due to the movement of the transmitter (Tx), the receiver (Rx) and the scatterers, the V2VRU channel is non-stationary [5]. Thus, the preferred approach to model the V2VRU channel is the GSCM approach as it is based on geometrical consideration [6].

In our GSCM channel modeling approach, dominant propagation paths are modeled deterministically by using the corresponding scatterers locations. These locations are drawn from statistical distributions, which in turn are obtained by analyzing the channel measurement data. Therefore, localizing the scatterers not only provides a deep understanding about the propagation channel, but also it is an essential step towards designing the channel model. The raw measurement data obtained from channel sounding cannot be used directly for a detailed characterization of the propagation channel when a GSCM approach is targeted. Therefore, a super resolution estimation algorithm can be employed to estimate the parameters of the MPCs. Few algorithms can be found in the literature like the snapshot-based RIMAX [8], and the space-alternating generalized expectation-maximization (SAGE) [9]. Alternatively, an algorithm that takes the evolution of the multipath overtime into account such as the Kalman enhanced super resolution tracking (KEST) [7] can be used.

Following the estimation of the parameters, MPCs have to be tracked over time. The tracking problem can also be seen as a labeling or data association problem. Several approaches for tracking and data association can be found in literature. Multipath component distance (MCD)-based approach is used in [10] and [11]. The authors in [12] applied probability hypothesis density (PHD) filters to track MPCs. Partitioning-based algorithms such as KPowerMeans is also used for data association and clustering in [13].

Having the MPCs tracked, a scatteres localization algorithm will use the estimated delay and Doppler of the tracked MPCs to relate each MPC to its corresponding scatterer in the propagation environment. Commonly, positions of scatterers are estimated based on a joint delay-Doppler estimation such as in [14], [15] and [16].

Few recent studies focused on modeling some aspects of the V2VRU channel. Rashdan et al. in [17] and [18] presented a narrowband channel model for the V2VRU channel considering a collision scenario between a vehicle and a pedestrian based on wideband channel measurements. The path loss was studied in [19] based on narrowband channel measurement in LoS when the pedestrian is stationary and moving parallel to the road. In [20], based on vehicle-to-pedestrian channel measurements in open-field environment, the authors localized the scatterers in the environment using a joint delay-Doppler estimation algorithm.

The main contributions and novelties of this work are summarized in the following:

1. We conducted an extensive wideband V2VRU channel measurement campaign in open-field and urban environments. The most critical accident prone scenarios that involve pedestrians and cyclists are considered.
2. We employ a super resolution estimation and tracking algorithm to estimate MPCs parameters.
3. We provide a novel method to extract specular reflections form the estimated time-variant CIR based on the density of their neighboring MPCs. This extraction allows for further characterization of the specular reflections.
4. We propose a simple but effective algorithm for multipath tracking based on delay and magnitude distance.
5. Locations of physical scatterers in the propagation environment are estimated using a joint delay-Doppler estimation algorithm. The locations will later be used to provide models for the statistical distribution of these scatterers.

The remainder of this paper is organized as follows: Section 2 describes the measurement campaigns in open-field and urban environments. Section 3 presents the results of MPCs parameters estimation and tracking. Within the section, a method to extract specular multipaths is presented followed by a detailed description of the MPCs tracking algorithm. Based on the tracked MPCs, Section 4 presents results on scatterers localization and the employed algorithm is described. Finally, a conclusion and summary in Section 5 concludes up the paper.

2 Measurement Campaigns

Since the goal is to model the V2VRU channel in critical scenarios, two extensive measurement campaigns have been conducted. The first measurement campaign was performed in 2017 on the runway of the airport in Oberpfaffenhofen near Munich, Germany. This location is selected since it represents an open-field environment and the acquired data can be used to develop a reference channel model. The second measurement campaign was conducted in 2018 in the city of Germering near Munich.

2.1 Measurement Scenarios

Open-field environment: LoS and NLoS scenarios were considered. All experiments were conducted with a receiver located at a moving pedestrian and a static tripod. Fig. 1 shows the trajectory of the test vehicle on an aerial view. Several scenarios were measured to cover the impact of different propagation aspects such as body shadowing, crowed shadowing, movement effect on the channel, and obstructions by parked vehicles. For more details on the measurement campaign, see [17]. In this work, results for only the LoS scenario with a static tripod (Fig. 2a) will be presented. In the scenario, the vehicle moved $100\,\mathrm{m}$ towards the imaginary collision point with an average speed of $11\,\mathrm{m/s}$, while the tripod was placed at $12\,\mathrm{m}$ distance from the collision point.

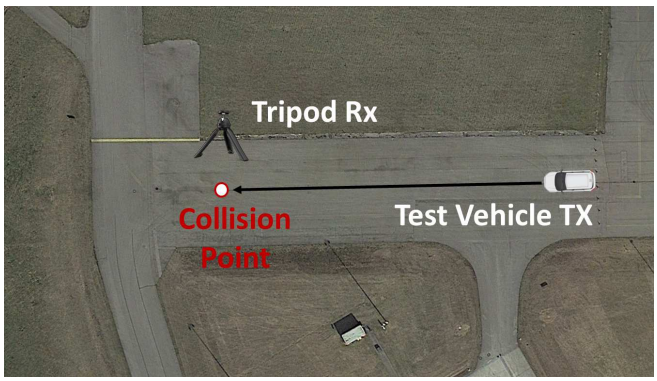

Fig. 1: Aerial view of the measurement scenario in the open-field environment showing the trajectory of the TX towards the imaginary collision point. (Google Maps 2017 Geobasis-DE/BKG.)

Table 1 Channel sounder parameters

Parameter	Value
RF center frequency f_c	5.2 GHz
Bandwidth B	120 MHz
Transmit power P_t	37 dBm
Signal period T_p in open-field	0.8 µs
Signal period T_p in urban	3.2 µs
Time grid T_g	1.024 ms
Tx antenna	Omni-directional (V-polarized), 8 dBi
Rx antenna	Omni-directional (V-polarized), 8 dBi

Urban environment: The measurements took place in three different urban streets. Pedestrian and cyclist accident scenarios were considered. In this work, we only investigate the channel measurements for the cyclist scenario in Göthestraße (see Fig. 3). Along the street, $3-$to $6-$story buildings are lined up on one side and separated by green areas on the other side. The street consists of one lane for each direction and contains parked vehicles on both sides. The street width is $12\,\mathrm{m}$ with $3\,\mathrm{m}$ wide sidewalks. In the cyclist accident scenario, as illustrated in Fig. 2b and 4, the vehicle is moving $100\,\mathrm{m}$ towards the intersection then turning right while the cyclist is moving $10\,\mathrm{m}$ toward the imaginary collision point from the right. This scenario accounts for $42\,\%$ of the total cyclist accidents as reported by the General Association of the German Insurance Industry (GDV) [2]. Also in this scenario, the visibility is blocked by buildings at the corner of the intersection and obstructed by parked vehicles. Fig. 3 displays the trajectories of the test vehicle, and the cyclist on an aerial view. The cyclist moves with an average velocities of $1.5\,\mathrm{m/s}$ while the test vehicle moves with a velocity between 5 and $11\,\mathrm{m/s}$.

2.2 Measurement Systems

The measurements were performed using the DLR RUSK channel sounder. The carrier frequency is $f_\mathrm{c} = 5.2\,\mathrm{GHz}$ and the bandwidth is $B = 120\,\mathrm{MHz}$, which corresponds to a delay resolution of $\Delta\tau = 8.33\,\mathrm{ns}$. During the measurements, the channel transfer function was recorded every $T_\mathrm{g} = 1.024\,\mathrm{ms}$, therefore, the maximum allowed absolute Doppler frequency is $f_{\mathrm{d\,max}} = 488\,\mathrm{Hz}$. Fig. 5 shows the antenna position on both the vehicle and the cyclist. The main measurement parameters of the channel sounder for both campaigns are summarized in Table 1.

(a) Open-field

(b) Urban

Fig. 2: Measurement environments.

Fig. 3: Aerial view of the measurement scenario in the urban environment showing the trajectory of the vehicle (in black), and the trajectory of the cyclist (in red) towards the imaginary collision point. (Google Earth 2018 Geobasis-DE/BKG.)

The measured CIRs for open-field and urban scenarios are shown in Fig. 6. At the beginning of the experiment, the Tx-Rx separation distance was approximately $100\,\mathrm{m}$. The LoS between the Tx and Rx was maintained in the open-field scenario with some traces parallel to the LoS. In the urban scenario, as can be seen in Fig. 6b, the LoS starts to appear, accompanied by a group of strong multipaths, at approximately $40\,\mathrm{m}$ distance or $12.5\,\mathrm{s}$. The LoS path remains between 12.5 and $19\,\mathrm{s}$ but is partially obstructed by parked vehicles. During NLoS, a weak path appears as a tail of the LoS path and with a slightly more delay than the geometric LoS (GLoS). A group of

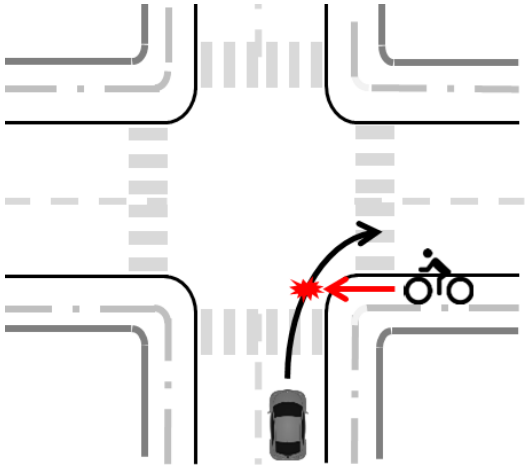

Fig. 4: An illustration of the accident scenario between a vehicle and a cyclist.

Fig. 5: Antennas positions on both the test vehicle and the cyclist.

weak paths can also be recognized. Contrary to the open-filed, in the urban measurements, the CIR is highly cluttered. This clutter consist of diffuse multipath components (DMCs),

3 Parameter Estimation and Tracking

In this section, based on the measurement data, the parameters of the MPCs will be estimated. Then, based on the estimated MPCs, the specular MPCs will be extracted and then tracked over time.

3.1 MPCs Parameter Estimation

The behavior of the multipath channel can be described by the time variant channel impulse response (CIR) $h(t_n, \tau)$ which can be expressed mathematically as a sum of $N(t_n)$ Dirac impulses [21]:

$$h(t_n, \tau) = \sum_{m=0}^{N(t_n)-1} \alpha_m(t_n) \cdot \delta_m(\tau - \tau_m(t_n)), \qquad (1)$$

where $\alpha_m(t_n)$ and $\tau_m(t_n)$ denote the complex amplitude and the delay of the m^{th} MPC in snapshot n and $\delta(\cdot)$ is a Dirac distribution. A dynamic multipath estimator named KEST, introduced in [7], is employed for estimating the parameters of specular MPCs. The estimated parameters are absolute value of the amplitude, the delay, and the phase of each MPC at time instant t_n. KEST uses the output of SAGE algorithm [9] as measurements within a Kalman filter. SAGE is used as a snapshot-based estimator that jointly estimates the complex amplitude $\alpha_m(t_n)$ and the delay $\tau_m(t_n)$ for each MPC m. Additional, KEST consists of several Kalman filters in parallel using different model orders for estimating the number of MPCs.

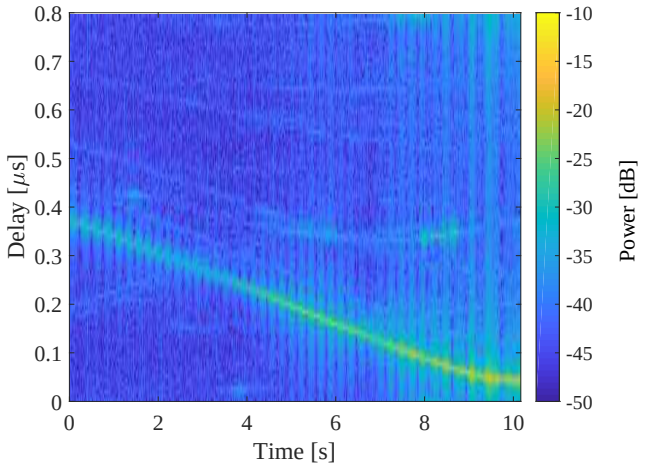

(a) Open-field

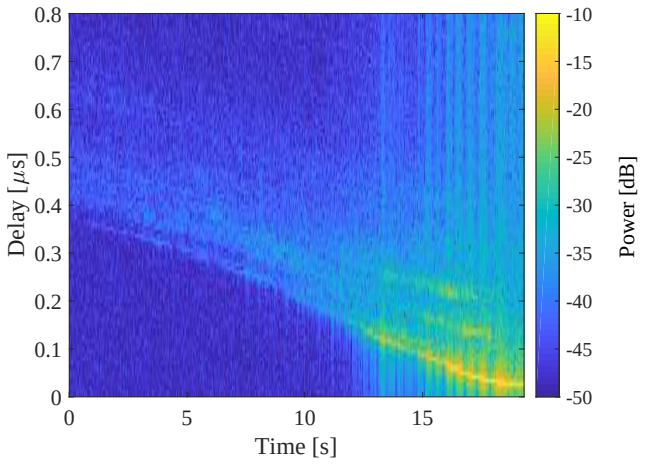

(b) Urban

Fig. 6: Time-variant CIRs based on the measured data.

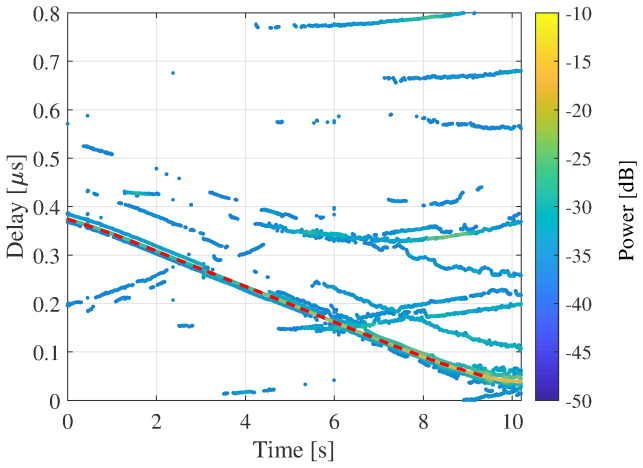

(a) Open-field

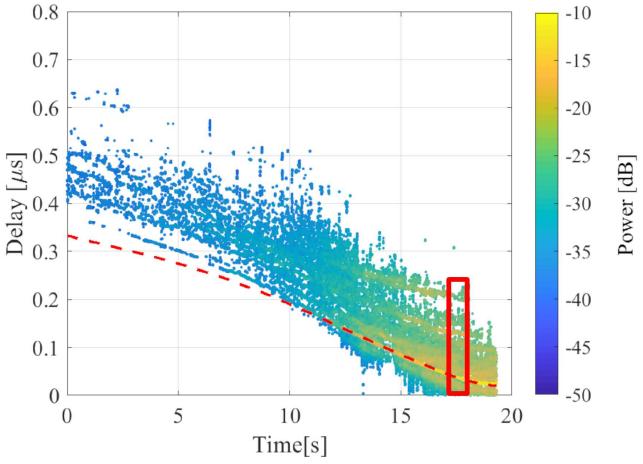

(b) Urban

Fig. 7: Time-variant CIRs based on the estimated parameters. The geometric LoS is displayed as a red dashed line.

Fig. 7 shows the CIRs for open-field and urban scenarios based on the estimated parameters by the KEST algorithm. The signal period T_{p} of the periodically transmitted multi-tone signal in the open-field environment was selected to be equal to $0.8\,\mu$s which corresponds to a propagation distance of $240\,\mathrm{m}$. Therefore, reflections with larger propagation distance were superimposed with the CIR of the next measurement snapshot. Nevertheless, the delay of these MPCs are corrected by adding $0.8\,\mu$s in the upcoming analyses. In the open-field environment, the LoS between the Tx and the Rx was never obstructed and, consequently, the first measured path coincides with the geometric LoS. However, in the urban environment, from 0 to $12.5\,\mathrm{s}$ the LoS was continuously obstructed by the building. Since the first path reaches the Rx after diffracting at its corner there is a misalignment between the first arriving path and the geometric LoS. At approximately $12.5\,\mathrm{s}$ or $40\,\mathrm{m}$ distance The Tx and Rx are in LoS.

It can be seen that, the estimation results in both scenarios confirm the initial observations made on the measured CIRs in the previous section. Based on the time-delay evolution structure of the MPCs, it can be deduced based on the long lifetimes that all paths in the estimated CIR in open-field are due to specular reflections. On the other hand, in the urban scenario, not only specular reflections but also DMCs can be seen. Therefore, in order to model the specular MPCs, we need to extract them form the estimated time-variant CIR.

3.2 Specular MPCs Extraction

Multipath components can be divided into specular reflections and diffuse scattering. we consider as specular reflections, paths that have relatively high power and long lifetime. Specular reflections are coherent, which means that they have a relatively constant phase difference with the direct path over time. While, on the other hand, DMCs will have random amplitudes and phases and therefore they are called incoherent components. Unlike specular reflections, DMCs have no clear structure in the time-delay domain and are often modeled as colored noise [8, 22]. Mirror-like smooth surfaces lead to only specular reflections and these reflections are also referred to as "strictly or smooth" reflections. Mirror-like surfaces are rarely found in outdoor environments and most surfaces possess some roughness (roughness in relation with the wavelength). The roughness will result in a decrease of the amplitude of the reflected path. This reduction is due to scattering some energy in different directions. The scattered energy is what called DMC. DMC is scattered from all or part of the rough surface and this part is called a glistening zone [23]. A very rough surface may result in canceling the contribution of the diffuse (incoherent) components. However, with a less rough surface, the DMCs contribute to the received signal and together with the specular (coherent) components produce an interference pattern on the path's amplitude.

Similar to the rough surfaces, vegetation also produces both specular reflections and DMCs [24, 25].

Table 2 Specular reflections extraction parameters

Parameter	Name	Value
δ	Search region radius	25 snapshots
$\zeta_{\Delta\tau}$	Delay difference threshold	1.5 ns
ζ_L	Nr. of neighbors threshold	10 MPCs

As seen in Fig. 7b, in the urban environment, the output of the MPCs parameters estimation not only contains specular reflections but also contains DMC. For channel modeling, the dominant specular multipath components with long lifetime need to be separated. DMC will not be neglected in our model since it may have a significant contribution to the total received power. However, modeling the DMC is out of the scope of this paper. In this work, we present a method to separate specular reflections and DMCs and based on their number of neighboring MPCs that have delay difference less or equal a specific threshold. The steps are summarized as follows:

0. For each MPC m in measurement snapshot n, a search radius δ is defined. The search region has a length of 2δ, and includes all snapshots with indices $n+p$, where $p = [-\delta, \ldots, -1, 1, 2, \ldots, \delta]$.
1. Check if the MPCs within the search region are close in delay as

$$T_{\tilde{m},n+p} = \begin{cases} 1 & \text{if } |\tau_{m,n} - \tau_{\tilde{m},n+p}| \leq \zeta_{\Delta\tau} \\ 0 & \text{otherwise,} \end{cases} \tag{2}$$

where $\tau_{m,n}$ is the delay of the MPC m in snapshot n at time instant t_n, $\tau_{\tilde{m},n+p}$ is the delay of the MPC $\tilde{m}$ in snapshot $n+p$, $\zeta_{\Delta\tau}$ is the delay difference threshold, "1" means the MPC under examination is close in delay, and "0" means it is not. The set $\boldsymbol{\mathcal{T}}$ is defined as

$$\boldsymbol{\mathcal{T}} = \{T_{\tilde{m},n+p} \mid p = -\delta, \ldots, -1, 1, 2, \ldots, \delta, \;\; \tilde{m} = 1, 2, \ldots, N_{n+p}\}, \tag{3}$$

where N_{n+p} is the number of MPCs in snapshot $n+p$.
2. The MPC is classified as specular or diffuse multipath as

$$\text{MPC} \widehat{=} \begin{cases} \text{Specular} & \text{if } \sum_{T_{\tilde{m},n+p} \in \boldsymbol{\mathcal{T}}} T_{\tilde{m},n+p} \geq \zeta_L, \\ \text{Diffuse} & \text{otherwise,} \end{cases} \tag{4}$$

where ζ_L is a threshold on the number of neighbors. The MPC is considered as specular if the number of detected MPCs in the region $t_{n-\delta}, \ldots, t_{n+\delta}$ and $\tau_{m,n} - \zeta_{\Delta\tau}, \ldots, \tau_{m,n} + \zeta_{\Delta\tau}$ is larger than or equal the threshold ζ_L.

3.2.1 Parameters Selection: The values of the thresholds ζ_L and $\zeta_{\Delta\tau}$ depend on the richness of the DMCs. These values affect the performance of the extraction and therefore should be carefully chosen. By decreasing $\zeta_{\Delta\tau}$ more specular MPCs with high delay variations will be mistakenly classified as DMCs. Contrarily, by increasing $\zeta_{\Delta\tau}$ more DMCs will be mistakenly classified as specular MPCs. In order to compare the effect of variations in the $\zeta_{\Delta\tau}$ parameter, specular MPCs extraction is performed with three different $\zeta_{\Delta\tau}$ values. Fig. 8 only shows the extracted specular MPCs for the part of the CIR within the red rectangle depicted in Fig. 7b. With larger $\zeta_{\Delta\tau}$ more MPCs are classified as specular MPCs.

Similarly, decreasing ζ_L will result in more DMCs that are mistakenly classified as specular MPCs. On the other hand, when increasing ζ_L more specular MPCs which have short lifetimes are also mistakenly classified as DMCs, although a MPC that has short lifetime could be a part of a longer but discontinuous path that is associated with one scatterer in the propagation environment. The aforementioned effect of the ζ_L parameter value on the specular MPCs extraction can be clearly seen in Fig. 9.

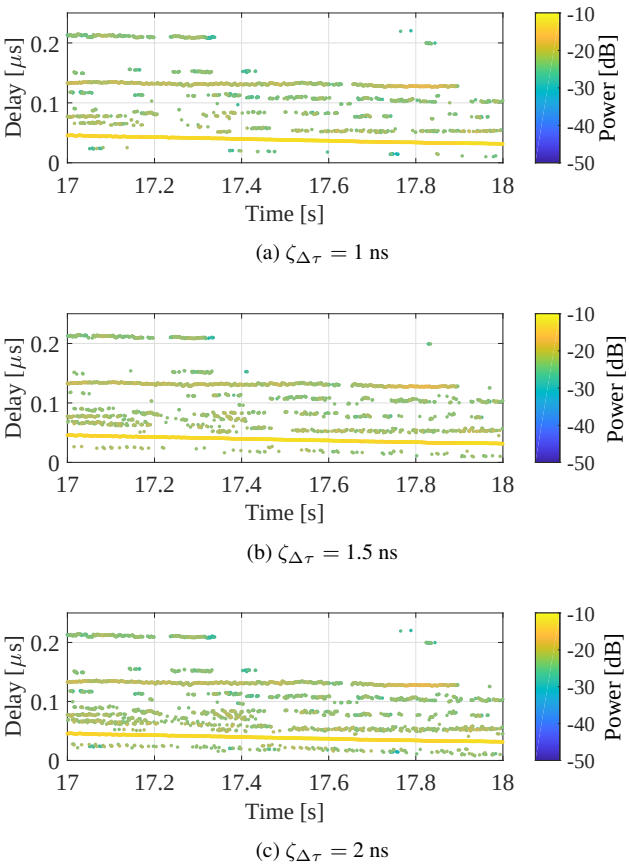

(a) $\zeta_{\Delta\tau} = 1$ ns

(b) $\zeta_{\Delta\tau} = 1.5$ ns

(c) $\zeta_{\Delta\tau} = 2$ ns

Fig. 8: The extracted specular MPCs using different values for $\zeta_{\Delta\tau}$ while $\zeta_L = 10$ MPCs and $\delta = 25$ snapshots.

The thresholds $\zeta_{\Delta\tau}$ and ζ_L should be chosen to minimize the specular MPCs to be mistakenly classified as DMCs. However, this will also result in some DMCs to be classified as specular MPCs. However, the misclassification of some DMCs as specular MPCs is affordable since their contribution to the total received power is marginal. Moreover, most of these misclassified MPCs can later be removed based on their short lifetimes in the tracking step.

The aforementioned method is applied on the estimated MPCs in urban environment from Fig. 7b. Fig. 10a shows the CIR based on the estimated parameters of the specular MPCs. The CIR of the residual after extracting the specular MPCs is shown in Fig. 10b. The values of the parameters used are summarized in Table 2.

3.3 Specular MPCs Tracking

Tracking the temporal evolution of the extracted specular MPCs is a prerequisite step to not only localize their scatterers using the phase changes, but also to determine their time-variant properties e.g., lifetime and visibility region. The KEST algorithm is able to continuously track each estimated MPC from Fig. 7a over time in the open-field scenario as visualized in Fig. 12. By visual inspection it can be seen that generally KEST algorithm correctly associates and tracks the MPCs over time. Especially stand-alone scattering points as A1-A3 and A9-A11 are well identified. However, the algorithm had difficulties in resolving A12 and A8/A13 when all three intersect in the Doppler/delay space. However, it is not able to track the paths for a long period of time in the urban scenario due to the richness of DMC. Therefore, we propose an MCD-based MPC tracking algorithm that utilizes the estimated delay and magnitude for tracking. We assume that in the same snapshot, the delay and magnitude of each MPC are unique, which means only one MPC with the same delay and magnitude exists. The main steps are as follows:

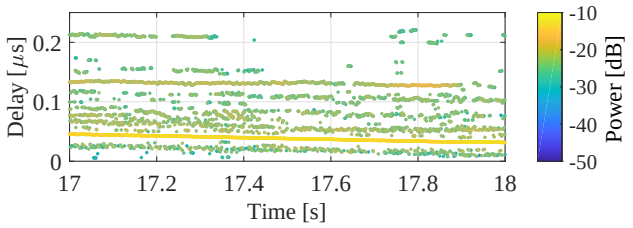

(a) $\zeta_L = 5$ MPCs

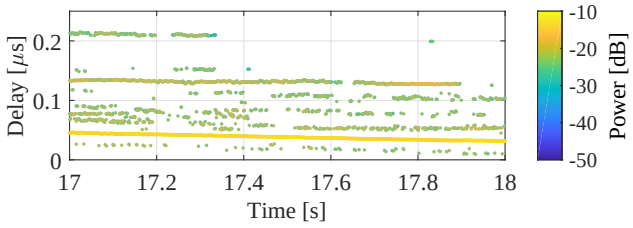

(b) $\zeta_L = 10$ MPCs

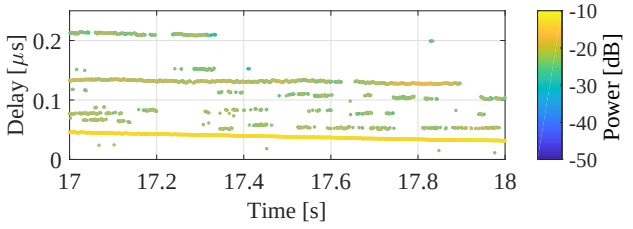

(c) $\zeta_L = 15$ MPCs

Fig. 9: The extracted specular MPCs using different values for ζ_L while $\zeta_{\Delta\tau}$ =1.5 ns and $\delta = 25$ snapshots.

0. Initialize the set of indices (labels) of all MPCs in the first snapshot $\boldsymbol{\mathcal{I}}_1 = \{1, 2, 3, \ldots, N_1\}$, Where N_1 is the number of MPCs in the snapshot $n = 1$. A delay difference threshold $\zeta_{\Delta\tau}$ is set to be equal to a predefined initial value $\zeta_{\Delta\tau\text{ini}}$. A magnitude difference threshold $\zeta_{\Delta\alpha}$ is also set to be equal to a predefined initial value $\zeta_{\Delta\alpha\text{ini}}$.

For each MPC $m = 1, 2, \ldots, N_n$ in the snapshot n, do:

1. Find the set of indices of the MPCs form the previous snapshot that have delay differences to $\tau_{i_{m,n}}$ less than or equal to the threshold $\zeta_{\Delta\tau}$.

$$\boldsymbol{\mathcal{A}}_{m,n} = \{i_{\tilde{m},n-1} \in \boldsymbol{\mathcal{I}}_{n-1} \big| \, |\tau_{i_{m,n}} - \tau_{i_{\tilde{m},n-1}}| \leq \zeta_{\Delta\tau}\}, \quad (5)$$

where $\boldsymbol{\mathcal{I}}_{n-1}$ is the set of all indices in the snapshot $n-1$, and $i_{\tilde{m},n-1}$ is the index (label) of the MPC $\tilde{m}$ in snapshot $n-1$.

2. Similarly, find the set of indices of the MPCs form the previous snapshot that have magnitude differences to $\alpha_{i_{m,n}}$ less than or equal to the threshold $\zeta_{\Delta\alpha}$.

$$\boldsymbol{\mathcal{B}}_{m,n} = \{i_{\tilde{m},n-1} \in \boldsymbol{\mathcal{I}}_{n-1} \big| \, |\alpha_{i_{m,n}} - \alpha_{i_{\tilde{m},n-1}}| \leq \zeta_{\Delta\alpha}\}, \quad (6)$$

for simplicity in notation, $\boldsymbol{\mathcal{A}}_{m,n} \widehat{=} \boldsymbol{\mathcal{A}}$ and $\boldsymbol{\mathcal{B}}_{m,n} \widehat{=} \boldsymbol{\mathcal{B}}$.

3. Let

$$\mathcal{C} = \underset{i_{\tilde{m},n-1} \in \boldsymbol{\mathcal{I}}_{n-1}}{\arg\min} \; |\tau_{i_{m,n}} - \tau_{i_{\tilde{m},n-1}}| \quad (7)$$

be the index (label) of the MPC that has a minimum delay difference to $\tau_{i_{m,n}}$. Only one MPC will have a minimum delay difference.

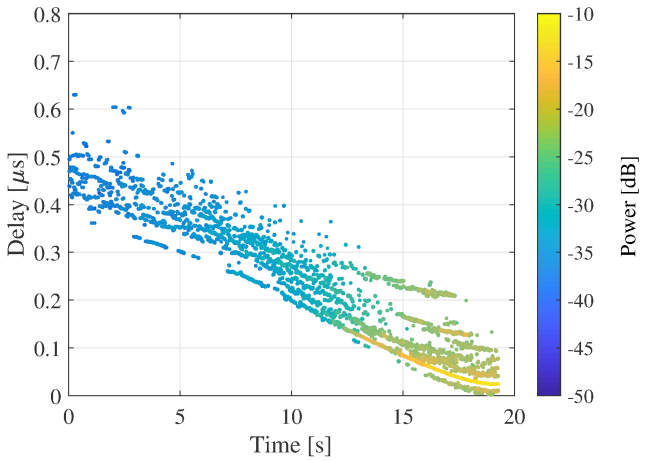

(a) Specular paths extracted form the estimated CIR.

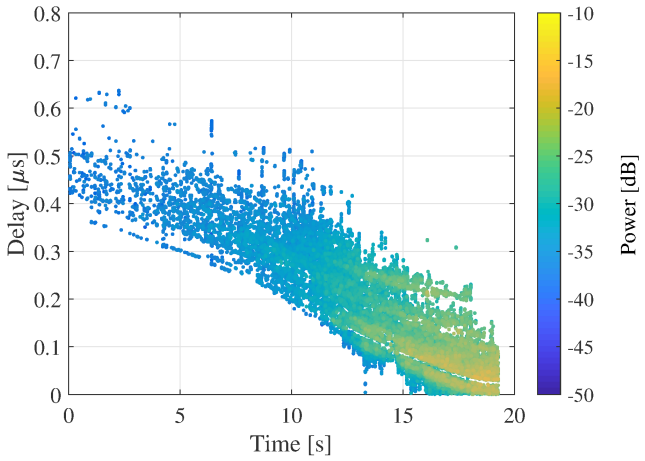

(b) The residual after extracting specular paths. The residual may contains DMC, noise, and artifacts.

Fig. 10: Results of the specular MPCs extraction method.

4. Similarly, let

$$\mathcal{D} = \underset{i_{\tilde{m},n-1} \in \boldsymbol{\mathcal{I}}_{n-1}}{\arg\min} \; |\alpha_{i_{m,n}} - \alpha_{i_{\tilde{m},n-1}}| \quad (8)$$

be the index of the MPC that has a minimum magnitude difference to $\alpha_{i_{m,n}}$. Only one MPC will have a minimum amplitude difference.

5. For each MPC m in each snapshot n, the values of both $\zeta_{\Delta\tau}$ and $\zeta_{\Delta\alpha}$ are updated as follows

a. If $\mathcal{C} = \mathcal{D}$, $\boldsymbol{\mathcal{A}} = \phi$ and $\boldsymbol{\mathcal{B}} \neq \phi$, where ϕ is an empty set, which means that there is a MPC that has both minimum delay difference and minimum magnitude difference. However, the delay difference is above the threshold. Therefore, the current threshold is increased as

$$\zeta_{\Delta\tau} = \begin{cases} |\tau_{i_{m,n}} - \tau_{n-1}(\mathcal{C})| & \text{if } |\tau_{i_{m,n}} - \tau_{n-1}(\mathcal{C})| < \zeta_{\Delta\tau\text{ini}} \\ \zeta_{\Delta\tau\text{ini}} & \text{otherwise} \end{cases} \quad (9)$$

where $\tau_{n-1}(\mathcal{C})$ is the delay of the MPC that has an index $\mathcal{C}$ in snapshot $n-1$. Which means that the delay difference threshold is set to be equal to the minimum difference if this minimum does not exceed the initial delay difference threshold. Otherwise, the threshold will be updated to be equal to the initial threshold.

The magnitude threshold is updated by a weighted average

$$\zeta_{\Delta\alpha} = \kappa_\alpha \overline{\Delta\alpha_k(\mathcal{D})}, \tag{10}$$

where $\Delta\alpha_k(\mathcal{D}) = |\alpha_k(\mathcal{D}) - \alpha_{k-1}(\mathcal{D})|$ is the absolute of the magnitude difference between two MPCs with the same index $\mathcal{D}$ in consecutive snapshots, $k = n-500, \ldots, n-1$ are the indices of the previous 500 snapshots, and $\kappa_\alpha > 1$ is a constant parameter. This means that the magnitude difference threshold is updated by the weighted average of the magnitude differences in the closest tracked path.

b. If $\mathcal{C} = \mathcal{D}$, $\boldsymbol{\mathcal{A}} \neq \phi$ and $\boldsymbol{\mathcal{B}} = \phi$, which means that there is a MPC that has both minimum delay difference and minimum magnitude difference. However, the magnitude difference is above the threshold. Therefore, the current magnitude threshold is increased as

$$\zeta_{\Delta\alpha} = \begin{cases} |\alpha_{i_{m,n}} - \alpha_{n-1}(\mathcal{C})| & \text{if } |\alpha_{i_{m,n}} - \alpha_{n-1}(\mathcal{C})| < \zeta_{\Delta\alpha\text{ini}} \\ \zeta_{\Delta\alpha\text{ini}} & \text{otherwise} \end{cases} \tag{11}$$

Similar to (a), the delay threshold is updated by a weighted average

$$\zeta_{\Delta\tau} = \kappa_\tau \overline{\Delta\tau_k(\mathcal{C})}, \tag{12}$$

where $\Delta\tau_k(\mathcal{C}) = |\tau_k(\mathcal{C}) - \tau_{k-1}(\mathcal{C})|$ is the absolute of the delay difference between two MPCs with the same index $\mathcal{C}$ in consecutive snapshots, $k = n-500, \ldots, n-1$ are the indices of the previous 500 snapshots, and $\kappa_\tau > 1$ is a constant parameter.

After updating the thresholds, the tracking begins as follows:

6. If $\boldsymbol{\mathcal{A}} \cap \boldsymbol{\mathcal{B}} \neq \phi$, one or more matching MPCs are found. If more than one matching MPCs are found, then select the one which has the least delay difference. If the index of the matching MPC is not already assigned to another MPC in the same snapshot n (step 7), then $\mathcal{I}_{m,n} = \boldsymbol{\mathcal{A}} \cap \boldsymbol{\mathcal{B}}$.
7. If $\boldsymbol{\mathcal{A}} \neq \phi$, $\boldsymbol{\mathcal{B}} \neq \phi$, and $\boldsymbol{\mathcal{A}} \cap \boldsymbol{\mathcal{B}} = \phi$, then there are at least two different MPCs, one of them satisfies the magnitude difference condition and the other satisfies the delay difference condition. In order to decide which MPC to choose, we calculate a choice metric γ for both choices as

$$\gamma_\tau = \omega_\tau \left(\frac{\zeta_{\Delta\tau}}{|\tau_{i_{m,n}} - \tau_{n-1}(\mathcal{C})|} \right) + \omega_\alpha \left(\frac{\zeta_{\Delta\alpha}}{|\alpha_{i_{m,n}} - \alpha_{n-1}(\mathcal{C})|} \right), \tag{13}$$

and

$$\gamma_\alpha = \omega_\tau \left(\frac{\zeta_{\Delta\tau}}{|\tau_{i_{m,n}} - \tau_{n-1}(\mathcal{D})|} \right) + \omega_\alpha \left(\frac{\zeta_{\Delta\alpha}}{|\alpha_{i_{m,n}} - \alpha_{n-1}(\mathcal{D})|} \right), \tag{14}$$

where $\omega_\tau + \omega_\alpha = 1$, and $\omega_\tau > 0, \omega_\alpha > 0$ are the weight parameters of the delay and magnitude, respectively. Based on the values of γ_τ and γ_α, the matching MPC is then selected as

$$i_{m,n} = \begin{cases} \mathcal{C} & \text{if } \gamma_\tau \geq \gamma_\alpha \\ \mathcal{D} & \text{if } \gamma_\alpha > \gamma_\tau. \end{cases} \tag{15}$$

Which means that matching MPC is the one that satisfies the delay condition if $\gamma_\tau \geq \gamma_\alpha$, or it is the one that satisfies the magnitude condition if $\gamma_\alpha > \gamma_\tau$. However, the selection is final only if the index of the matching MPC is not already assigned another MPC in the same snapshot n (step 8).
8. If the index of the matching MPC is already selected by another MPC with a delay $\tau_{i_{l,n}}$, then the delay of both MPCs will be compared with $\tau_{n-1}(\mathcal{C})$. The MPC with the least delay difference will be assigned the index $\mathcal{C}$ while the other MPC will search for a match within the previous δ_p snapshots (step 10), where δ_p is a constant parameter corresponds to the length of the search region,

$$i_{m,n} = \begin{cases} \mathcal{C} & \text{if } |\tau_{i_{m,n}} - \tau_{n-1}(\mathcal{C})| < |\tau_{i_{l,n}} - \tau_{n-1}(\mathcal{C})|, \\ \text{Search back (step 10)} & \text{otherwise,} \end{cases} \tag{16}$$

and consequently,

$$i_{l,n} = \begin{cases} \mathcal{C} & \text{if } |\tau_{i_{l,n}} - \tau_{n-1}(\mathcal{C})| < |\tau_{i_{m,n}} - \tau_{n-1}(\mathcal{C})|, \\ \text{Search back (step 10)} & \text{otherwise.} \end{cases} \tag{17}$$

9. If $\boldsymbol{\mathcal{A}} = \phi$ or $\boldsymbol{\mathcal{B}} = \phi$, then there is no match in the previous snapshot. Therefore, the MPC will search for a match within the previous δ_p snapshots (step 10).
10. Search Back: When the MPC does not find a match from the previous snapshot, then it searches for a match within a window of length δ_p snapshots. For each MPC in each snapshot in the search window, the distance metric is calculated as,

$$S_{\tilde{m},n-p} = \sqrt{\omega_\tau \left(\frac{\tau_{i_{m,n}} - \tau_{i_{\tilde{m},n-p}}}{\tau_{i_{m,n}}} \right)^2 + \omega_\alpha \left(\frac{\alpha_{i_{m,n}} - \alpha_{i_{\tilde{m},n-p}}}{\alpha_{i_{m,n}}} \right)^2}, \tag{18}$$

where $\boldsymbol{\mathcal{S}}_p = \{S_{\tilde{m},n-p} | p = 2, 3, , \ldots, \delta_p + 1\}$ is a set of all distances $S_{\tilde{m},n-p}$, and $p = 2, 3, , \ldots, \delta_p + 1$. The matching MPC is selected as follows:

$$i_{m,n} = \begin{cases} i_{\tilde{m},n-p} & \text{if } S_{\tilde{m},n-p} = \min(\boldsymbol{\mathcal{S}}_p) \\ \text{new path} & \text{otherwise,} \end{cases} \tag{19}$$

If a matching path is found go to (step 8), and if the path is considered as a new path, it will get a new index.

The parameters values used for tracking are summarized in Table 3.

3.3.1 Parameters Selection: One important problem that affects the performance of algorithms is parameters tuning. The parameter tuning procedure could be long and time consuming. Our tracking algorithm will only require minimum offline tuning efforts. In our tracking algorithm, 7 parameters, listed in Table 3, need to be initialized, and two parameters, namely, the delay difference threshold $\zeta_{\Delta\tau}$ and the magnitude difference threshold $\zeta_{\Delta\alpha}$ are tuned automatically. The measured delay differences $|\tau_{i_{m,n}} - \tau_{i_{\tilde{m},n-1}}|$ and the updated delay threshold for the LoS path are shown in Fig. 11a. The updated threshold is upper-bounded by the initial threshold $\zeta_{\Delta\tau\text{ini}} = 10\,\text{ns}$ and its value for each MPC in each snapshot is updated as in step 5. Similarly, the measured magnitude differences $|\alpha_{i_{m,n}} - \alpha_{i_{\tilde{m},n-1}}|$ and the updated magnitude threshold for the LoS path are shown in Fig. 11b

The initial thresholds $\zeta_{\Delta\tau\text{ini}}$ and $\zeta_{\Delta\alpha\text{ini}}$ represent upper bounds on the delay and amplitude changes between two consecutive measurement snapshots. The selection of their values does not require extensive tuning. It is only important to choose values larger than the average delay and amplitude changes between two consecutive measurement snapshots. For example with average delay change of $0.5\,\text{ns}$, any value between $5-10\,\text{ns}$ is suitable. Similarly, with an average magnitude change of $0.15\,\text{dB}$, any value between 1.5 and $3\,\text{dB}$ is suitable. The constants parameter κ_τ is used to update the delay threshold in Step 5b. As a rule of thumb, it has been found that any value between 5 and 10 is suitable. However, if fine tuning is preferred, the selection of the value can be done by an initial tracking step using arbitrary large values ≥ 10. In this initial tracking, the LoS can be easily tracked because of its high power and smooth delay evolution over time. Based on the delay changes within the tracked LoS path, the weighting constants is tuned to be large enough such that the updated threshold is larger than the delay difference of the tracked LoS and small enough to not exceed the initial threshold. Similar procedure is also applied to tune κ_α.

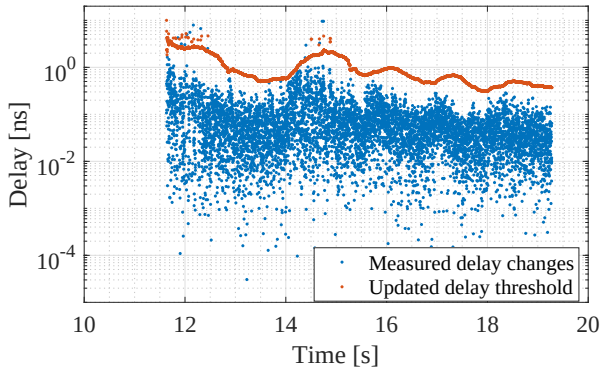

(a) Delay threshold update

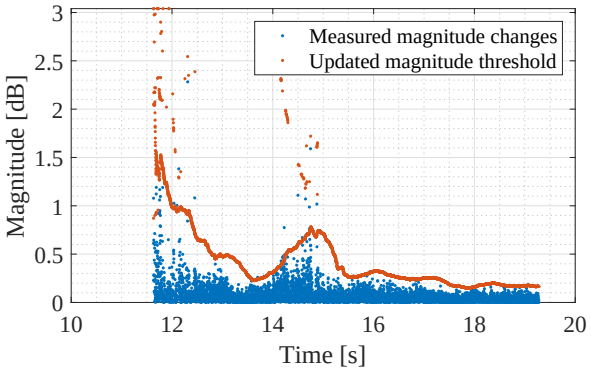

(b) Magnitude threshold update

Fig. 11: The automated tuning of the delay and magnitude threshold for the LoS component.

Table 3 Tracking parameters

Parameter	Name	Value
$\zeta_{\Delta\tau\,\mathrm{ini}}$	Initial delay difference threshold	10 ns
$\zeta_{\Delta\alpha\,\mathrm{ini}}$	Initial magnitude difference threshold	3.04 dB
κ_τ	Tuning constant for delay difference threshold	10
κ_α	Tuning constant for magnitude difference threshold	5
ω_τ	Delay weight	0.9
ω_α	Magnitude weight	0.1
δ_p	Search range	100 snapshots

When the algorithm need to decide between two MPCs, one only satisfies the delay condition while the other only satisfies the power condition, the weighting constants ω_τ and ω_α become useful. Higher delay weight means that the delay similarity is preferred over the power similarity. The selection of the weights values depends on the objective of the tracking and on the data. In our problem, due to the fact that paths with difference delay may have similar power and the objective is to track the evolution of MPCs over time, larger delay weight is selected.

Fig. 15 displays the results of the specular MPC tracking for the urban environment of Fig. 7b. In the first part of the measurements until 12.5 s where Tx and Rx were in NLoS condition, the algorithm succeeds in tracking the signal diffracted by the obstructing building (B7). However it is unable to find singular MPCs that can be tracked over longer periods of time inside the (B1) cloud. In the LoS situation, when stronger and more discrete MPCs appear, the algorithm is again able to track some strong MPCs, as for instance (B2, B3 and B5). These MPCs appear divided in different chunks. If they belong to the same or to different objects will be assessed in the next section. The accuracy of scatterers localization in Section 4 can be considered as an indication of the performance of the proposed tracking algorithm.

4 Scatterers Localization

The estimated delay τ and Doppler ν, based on the phase of the estimated complex amplitude, are used to localize scatterers in the propagation environment. For the sake of simplicity we represent the objects as a source of single bounce reflection. A two-dimensional Cartesian coordinate system is considered to describe the propagation scenario. The LoS and the scattered components are assumed to propagate horizontally. This means that the differences in antenna heights and the scattering point height are neglected and the scatterers are then located on a ground plane together with the Tx and Rx antennas. The delay τ of a MPC depends on the Tx position $\mathbf{T}$, the Rx position $\mathbf{R}$, and the scatterer position $\mathbf{S}$, and it is given by

$$\tau = \frac{1}{\mathrm{c}} \left(\|\mathbf{S} - \mathbf{T}\| + \|\mathbf{R} - \mathbf{S}\| \right), \tag{20}$$

where c is the speed of light.

When only Tx or Rx is moving, the Doppler frequency ν in the 2-dimensional Cartesian coordinate system has a shape of a hyperbola. However, if both Tx and Rx are moving, the Doppler frequency has no typical shape any more. The Doppler frequency is given by

$$\nu = \frac{f_\mathrm{c}}{\mathrm{c}} \left(v_\mathrm{T} \frac{\mathbf{S} - \mathbf{T}}{\|\mathbf{S} - \mathbf{T}\|} + v_\mathrm{R} \frac{\mathbf{R} - \mathbf{S}}{\|\mathbf{R} - \mathbf{S}\|} \right), \tag{21}$$

where v_T and v_R are the velocity of Tx and Rx, respectively. In this representation, the scatterer location is calculated by intersecting the curves represented by τ and ν. The intersection results in two points on the ellipse given by (20). Only one of them is the true scattering point location while the other is an ambiguity. In this work, we adopt the localization algorithm from [15] where scatterer location in each snapshot n and MPC m is calculated as a PDF. τ and ν are jointly expressed as a bivariate normal distribution, i.e., $\mathbf{K}(\boldsymbol{\theta}) \sim \mathcal{N}(\boldsymbol{\mu}, \boldsymbol{\Sigma})$ in the parameter space $\boldsymbol{\theta}$

$$\boldsymbol{\theta} = \begin{bmatrix} \tau \\ \nu \end{bmatrix}, \tag{22}$$

where

$$\boldsymbol{\mu} = \begin{bmatrix} \mu_\tau \\ \mu_\nu \end{bmatrix}, \tag{23}$$

is the mean values, and

$$\boldsymbol{\Sigma} = \begin{bmatrix} \sigma_\tau^2 & 0 \\ 0 & \sigma_\nu^2 \end{bmatrix}, \tag{24}$$

is the covariance matrix which is calculated from the estimated parameters in Section 3.1 assuming that τ and ν are independent. The joint PDF of the parameter $\boldsymbol{\theta}$ is given by

$$p(\boldsymbol{\theta}; \boldsymbol{\mu}, \boldsymbol{\Sigma}) = \frac{1}{2\pi\sigma_\tau\sigma_\nu} \exp\left(-\frac{(\tau - \mu_\tau)^2}{2\sigma_\tau^2} - \frac{(\nu - \mu_\nu)^2}{2\sigma_\nu^2} \right). \tag{25}$$

The next step is to transform the PDF $p(\boldsymbol{\theta}; \boldsymbol{\mu}, \boldsymbol{\Sigma})$ from the parameter domain into a Cartesian domain as

$$p(\boldsymbol{X}) = \frac{1}{N} p(\boldsymbol{\theta}) |\mathbf{J}|, \tag{26}$$

where N is the number of intersections between the shape defined by τ and the shape defined by ν, $\boldsymbol{X} = [x, y]^\mathrm{T}$, and $\mathbf{J}$ is the Jacobian of $\boldsymbol{\theta}$

$$\mathbf{J} = \det\left(\begin{bmatrix} \frac{\partial\tau}{\partial x} & \frac{\partial\tau}{\partial y} \\ \frac{\partial\nu}{\partial x} & \frac{\partial\nu}{\partial y} \end{bmatrix} \right). \tag{27}$$

The PDFs of the same MPC are then averaged over the lifetime of the MPC. During the movement of Tx and Rx, the ambiguities change

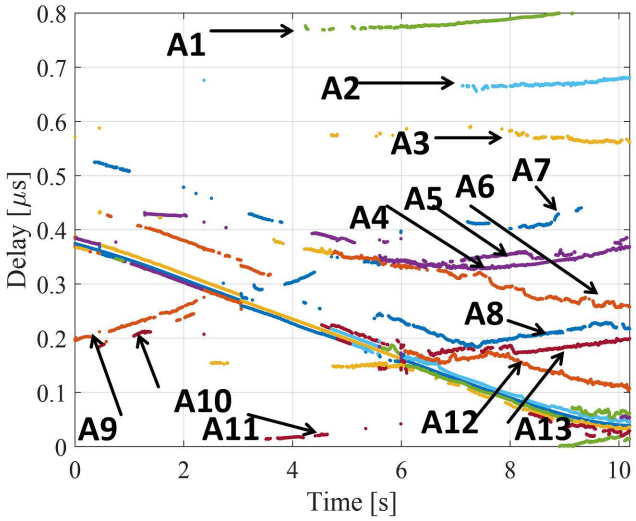

Fig. 12: Tracked path over time in open-field environment as a results of KEST algorithm.

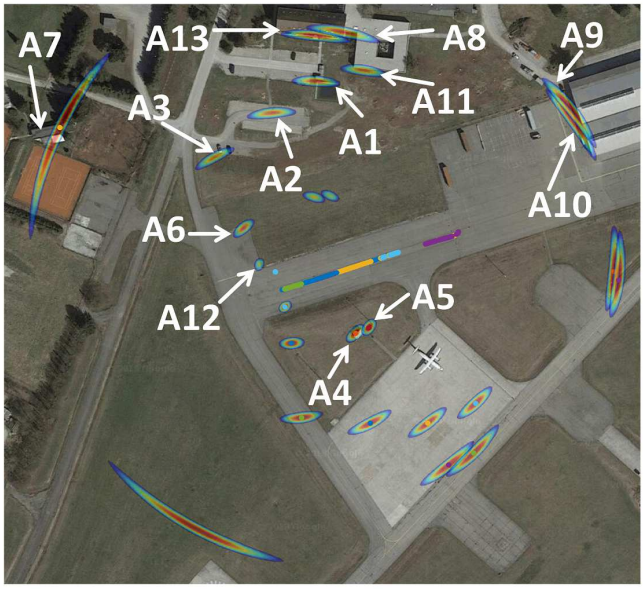

Fig. 13: Estimated Locations of the scatterers in open-field scenario. The results not only show the true locations but also the ambiguities. The trajectories of the Tx and the Rx are shown © Google.

their locations while the true locations remains fixed. As a result of the averaging, the ambiguities are partially or completely averaged out.

Fig. 13 shows the estimated locations of scatterers in the open-field environment, and the photos of the scatterers are shown in Fig. 14 . Our purpose of showing the results of scatterers localization in open-field environment is to show the performance of the localization algorithm in controlled environment and under perfect GNSS reception and low multipath interference. The results show that the localization algorithm is able to accurately localize the scatterers. The PDFs which are marked by arrows represent the PDFs of the true location. Other PDFs represent the ambiguities. Since only the Tx is moving, while the Rx is static, the ambiguities do not change their position and therefore they do not average out. At large Tx-Rx separation distance, reflection occurs on the hangers (A9 and A10). As the vehicle approaches the collision point, other scatterers become active such as the parked vehicles in the parking lots (A1, A2, and A3), a small room with metal walls (A4) and a nearby metal electric box (A5). Far office buildings (A8, A11, A13, and A7) are

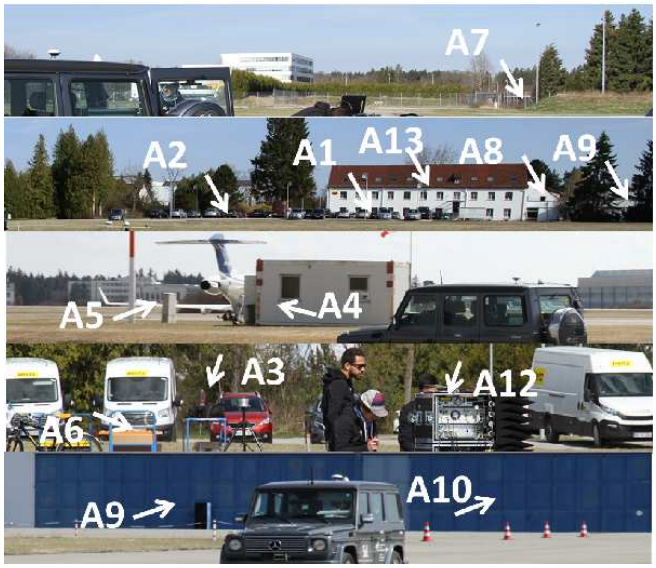

Fig. 14: Photos of the localized scatterers in the open-field environment.

also identified as reflection sources. A12 and A6 are the position of the channel sounder and the nearby trolleys respectively.

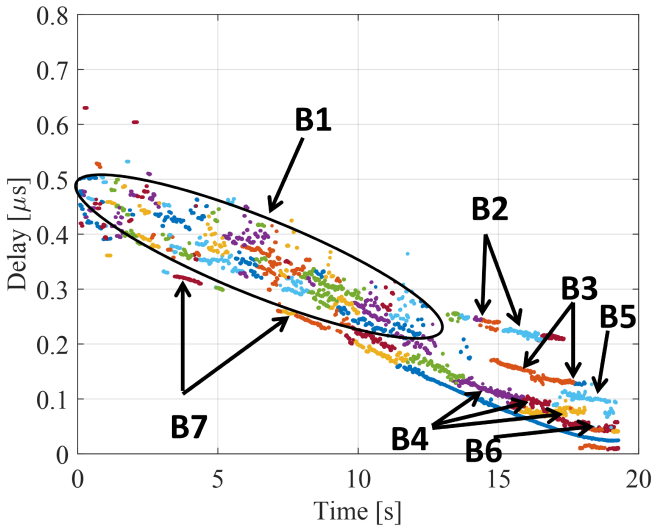

Fig. 15: Tracked path over time in urban environment as a results of the proposed tracking algorithm.

The estimated locations of the scatterers in urban environment are shown in Fig. 16. Different objects in the environment could be identified as sources of reflections and scattering as a result of the localization algorithm. In NLoS situation, several short MPCs (B1) in Fig. 15 reach the receiver after scattering from tree branches and leaves as shown in Fig. 16a and Fig. 17. The lampposts and the traffic signs under the trees canopy (B1) could also be sources of reflections during NLoS situation. It can be seen that the ambiguities are partially averaged. Despite the existence of several objects, such as parked card, traffic signs, and the corner building, that have visibility to both the Tx and the Rx, no MPCs are received from these objects. Simply, In NLoS scenario the location of these objects and the position of Tx and Rx do not satisfy the low of reflection.

Single and double-bounce specular reflections from the surrounding objects in the environment in LoS situation are observed. The estimated locations of the single bounce reflections (B3) are not exactly on the facade of the building but rather $1-2\,\mathrm{m}$ behind it as shown in Fig. 16b. One reason could be the inaccuracy of GNSS

(a) NLoS

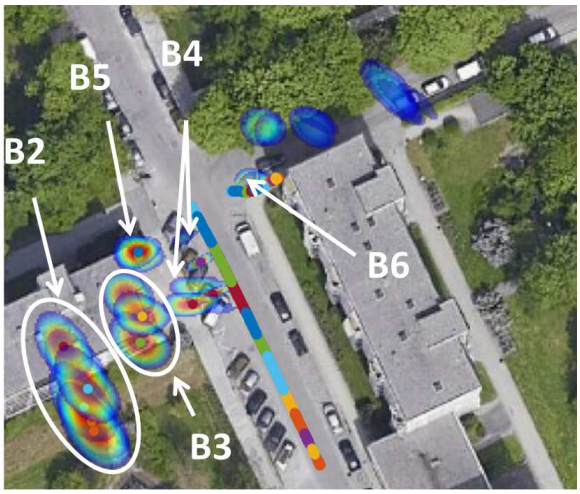

(b) LoS

Fig. 16: Estimated Locations of the scatterers in the urban scenario. The results not only show the true locations but also the ambiguities. The trajectories of the Tx and the Rx are shown © Google. At each time instant, the trajectories of the Tx and Rx together with the point in the center of the location PDF have the same color.

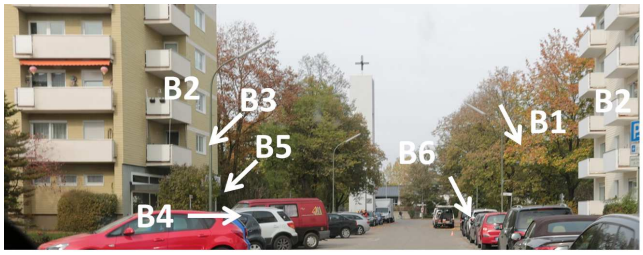

Fig. 17: Photos of the localized scatterers in the urban environment.

data. However, according to our assumption, the reflection point together with the Tx and Rx antennas are located on the same horizontal plane. Therefore, when the actual height of the reflection point doesn't comply with the assumption, the estimated location will appear in front of or behind the facade of the reflectors. In our scenario, (B3) MPCs are most probably generated by reflections from the metallic balconies of the first floor. The estimated locations of the MPCs (B2) appear to be about 15 m behind the building facade. It has been found, by simple ray-tracing, that MPCs (B2) are generated by double bounce reflections from the right then the left buildings. In addition to the single and double-bounce reflections from the right and left building, reflections from several parked cars (B4) on the left side of the road and from a car (B6) at the corner near to the cyclist are also observed. Moreover, the metallic shop sign is found to the source of reflections (B5).

5 Conclusion and Future Work

In this work, we performed wideband V2VRU channel measurement campaigns in open-field and urban environments. Critical collision scenarios involving pedestrians and cyclists are considered. The main aim of this paper is to localize scatterers in the propagation environment. Therefore, MPCs parameters are estimated by the KEST algorithm. According to the results of the parameter estimation in the urban environment, it is found that not only specular reflections are estimated but also part of the DMC is mistakenly estimated as specular reflections. Therefore, we proposed a method to extract the specular reflections and separate them from the DMC. Furthermore, we proposed a novel algorithm to track and label specular MPCs. Each path is then related to a physical scatterer by joint delay-Doppler estimation algorithm. Single and double bounce reflections from buildings and parked vehicles are identified in LoS situation. In NLoS situation, scattering from trees nearby the receiver as well as reflections from traffic signs and lampposts beneath the tree canopy are identified.

As a future work, we intend to localize scatterers in other urban streets for pedestrian and cyclist scenarios. The goal is to model scatterers locations by statistical distributions. Moreover, the lifetime and visibility angle for the scatterers are to be modeled.

6 References

[1] 'Road traffic injuries'. (Available from: http://www.who.int/violence_injury_prevention/road_traffic/en/

[2] Kuehn, M., Hummel, T., Lang, A. 'Cyclist-car accidents–their consequences for cyclists and typical accident scenarios'. In: Proceedings of the 24th International Conference on the Enhanced Safety of Vehicles, 2015.

[3] Molisch, A.F., Tufvesson, F., Karedal, J., Mecklenbrauker, C.F.: 'A survey on vehicle-to-vehicle propagation channels', *IEEE Wireless Communications*, 2009, **16**, (6), pp. 12–22

[4] Viriyasitavat, W., Boban, M., Tsai, H., Vasilakos, A.: 'Vehicular communications: Survey and challenges of channel and propagation models', *IEEE Vehicular Technology Magazine*, 2015, **10**, (2), pp. 55–66

[5] Bernado, L., Zemen, T., Tufvesson, F., Molisch, A.F., Mecklenbräuker, C.F.: 'Delay and Doppler spreads of nonstationary vehicular channels for safety-relevant scenarios', *IEEE Transactions on Vehicular Technology*, 2014, **63**, (1), pp. 82–93

[6] Molisch, A.F., Kuchar, A., Laurila, J., Hugl, K., Schmalenberger, R.: 'Geometry-based directional model for mobile radio channels—principles and implementation', *European Transactions on Telecommunications*, 2003, **14**, (4), pp. 351–359

[7] Jost, T., Wang, W., Fiebig, U.C., Perez.Fontan, F.: 'Detection and tracking of mobile propagation channel paths', *IEEE Transactions on Antennas and Propagation*, 2012, **60**, (10), pp. 4875–4883
[8] Thomä, R., Landmann, M., Richter, A. 'RIMAX-a maximum likelihood framework for parameter estimation in multidimensional channel sounding'. In: Proceedings of the International Symposium on Antennas and Propagation (ISAP'04). (Citeseer, 2004. pp. 53–56
[9] Fleury, B.H., Tschudin, M., Heddergott, R., Dahlhaus, D., Pedersen, K.I.: 'Channel parameter estimation in mobile radio environments using the SAGE algorithm', *IEEE Journal on selected areas in communications*, 1999, **17**, (3), pp. 434–450
[10] Karedal, J., Tufvesson, F., Czink, N., Paier, A., Dumard, C., Zemen, T., et al.: 'A geometry-based stochastic MIMO model for vehicle-to-vehicle communications', *IEEE Transactions on Wireless Communications*, 2009, **8**, (7), pp. 3646–3657
[11] Mahler, K., Keusgen, W., Tufvesson, F., Zemen, T., Caire, G.: 'Tracking of wideband multipath components in a vehicular communication scenario', *IEEE Transactions on Vehicular Technology*, 2016, **66**, (1), pp. 15–25
[12] Froehle, M., Meissner, P., Witrisal, K. 'Tracking of UWB multipath components using probability hypothesis density filters'. In: 2012 IEEE International Conference on Ultra-Wideband. (IEEE, 2012. pp. 306–310
[13] Czink, N., Cera, P., Salo, J., Bonek, E., Nuutinen, J.P., Ylitalo, J. 'A framework for automatic clustering of parametric MIMO channel data including path powers'. In: IEEE Vehicular Technology Conference. (IEEE, 2006. pp. 1–5
[14] Unterhuber, P., Walter, M., Schneckenburger, N., Kürner, T. 'Joint delay and Doppler frequency estimation for scatterer localization in railway environments'. In: 2019 13th European Conference on Antennas and Propagation (EuCAP). IEEE, 2019. pp. 1–5
[15] Schneckenburger, N., Jost, T., Shutin, D., Walter, M., Del.Galdo, G., Fiebig, U.C.: 'Reflector localization for geometrical modeling the air-ground channel', *IEEE Transactions on Vehicular Technology*, 2018,
[16] Lehner, A. (2007). Multipath channel modelling for satellite navigation systems. Shaker.
[17] Rashdan, I., de Ponte.Müller, F., Wang, W., Schmidhammer, M., Sand, S. 'Vehicle-to-pedestrian channel characterization: Wideband measurement campaign and first results'. In: IEEE 12th European Conference on Antennas and Propagation (EuCAP). London, UK, 2018.
[18] Rashdan, I., Müller, F.D.P., Jost, T., Sand, S., Caire, G.: 'Large-scale fading characteristics and models for vehicle-to-pedestrian channel at 5-GHz', *IEEE Access*, 2019, **7**, pp. 107648–107658
[19] Doone, M.G., Cotton, S.L., Matolak, D.W., Oestges, C., Heaney, S.F., Scanlon, W.G.: 'Pedestrian-to-vehicle communications in an urban environment: Channel measurements and modeling', *IEEE Transactions on Antennas and Propagation*, 2018, **67**, (3), pp. 1790–1803
[20] Rashdan, I., de Ponte.Müller, F., Jost, T., Sand, S. 'Measurement-based geometrical characterization of the vehicle-to-pedestrian channel'. In: 2019 13th European Conference on Antennas and Propagation (EuCAP). (IEEE, 2019. pp. 1–5
[21] Turin, G.L., Clapp, F.D., Johnston, T.L., Fine, S.B., Lavry, D.: 'A statistical model of urban multipath propagation', *IEEE Transactions on Vehicular Technology*, 1972, **21**, (1), pp. 1–9
[22] Jost, T., Wang, W., Shutin, D., Antreich, F. 'Using an autoregressive model for DMC'. In: 2012 6th European Conference on Antennas and Propagation (EUCAP). (IEEE, 2012. pp. 3504–3508
[23] Beckmann, P., Spizzichino, A.: 'The scattering of electromagnetic waves from rough surfaces', *Norwood, MA, Artech House, Inc, 1987, 511 p*, 1987,
[24] Savage, N., Ndzi, D., Seville, A., Vilar, E., Austin, J.: 'Radio wave propagation through vegetation: Factors influencing signal attenuation', *Radio Science*, 2003, **38**, (5)
[25] Al-Nuaimi, M. O., and A. M. Hammoudeh. "Measurements and predictions of attenuation and scatter of microwave signals by trees." IEE Proceedings-Microwaves, Antennas and Propagation 141.2 (1994): 70-76.